PAPER

Check for updates

Kinetics or thermodynamics? Extolling their role to modulate the crystal phases and luminescence of KY₃F₁₀:Eu³⁺ powders†

Pablo Serna-Gallén, [iD]* Héctor Beltrán-Mir [iD] and Eloísa Cordoncillo [iD]

KY₃F₁₀, a fluoride compound with two polymorphs (α and δ), has been a subject of study due to its unique properties. Obtaining the metastable δ-phase has been challenging, but this study presents an enhanced synthetic methodology using coprecipitation to isolate specific crystal phases. Varying the reaction temperature and time allows for the modulation of polymorph formation. The structural analysis of the synthesized powders reveals the influence of kinetic and thermodynamic control. The morphology of the particles is also affected by these factors, with different reaction conditions leading to distinct particle shapes. The luminescent response of Eu³⁺-doped powders helps understand the structural stability. It is demonstrated that time-resolved fluorescence spectroscopy is a sensitive and direct measurement to follow the observed changes. Overall, this study demonstrates the interplay between thermodynamics and kinetics in materials synthesis and the impact on crystal phase formation and properties.

1. Introduction

When it comes to materials synthesis, the corresponding thermodynamic phase diagram should be used as a starting point to yield the most stable product. However, it is not difficult to find some crystal phases that, although predicted as thermodynamically stable, cannot be synthesized experimentally and, instead of them, metastable phases are formed.[1–3] This fact evinces the competitive nature between the thermodynamic and the kinetic factors.

Thermodynamics is the cornerstone of materials and solids engineering because it helps us to study, predict, and explain the existence of different crystal phases, their range of stabilities, and their physicochemical properties.[4] On the other hand, the kinetics of a given chemical system involves the study of the concentration of reagents, reaction medium, pressure, temperature, catalysts, *etc.* that affect the reaction time or the formation of a specific product to the detriment of others. Given that, designing new synthetic approaches becomes a powerful strategy to tune the reaction pathways and thus the formation of the final product. Commonly, kinetic/metastable products (which are less stable thermodynamically) are favored under reaction conditions of low temperatures.[5] In contrast, high temperatures or pressures facilitate stabilizing thermodynamic products.[6,7]

In materials science, the controlled synthesis of polymorphs (*i.e.*, compounds with the same chemical formula but different crystal phases) has attracted significant interest because it opens up a plethora of possibilities regarding the functionalization and applications of solid materials.[8,9] However, understanding the involved crystal phase transformations is still a challenge in some compounds.[10,11]

In that sense, the KY₃F₁₀ host lattice emerges as a fluoride that deserves special attention. This compound presents two polymorphs with cubic structure[12,13] but completely different properties: the thermodynamic α-phase and the metastable δ-phase. Indeed, a δ → α phase transformation is observed around 440 °C,[14] thus corroborating the higher thermodynamic stability of α-KY₃F₁₀. α-KY₃F₁₀ crystallizes in a fluorite-type cubic structure with the $Fm\bar{3}m$ (no. 225) space group (SG). The lattice parameter is a = 11.536 Å, and the cell volume is V = 1535.20 Å³ with 8 formula units per unit cell (Z = 8).[12] The structure can be described by means of square antiprisms formed by YF₈ units, having the Y³⁺ central cation a C_{4v} local symmetry, Fig. 1(a). On the other hand, the δ-KY₃F₁₀·xH₂O compound has also a cubic structure with a similar SG = $Fd\bar{3}m$ (no. 227), Z = 16, and a = 15.492 Å (cell volume V = 3717.90 Å³).[14] The crystal structure is also composed of YF₈ square antiprisms, having the Y³⁺ central cation a C_{2v} local symmetry (*e.g.*, a symmetry lower than in α-KY₃F₁₀) Fig. 1(b). Additionally, the δ-phase incorporates crystalline water molecules which gives rise to a zeolitic behavior in this unique phase.

Departamento de Química Inorgánica y Orgánica, Universitat Jaume I, Av. Sos Baynat s/n 12071, Castelló de la Plana, Spain. E-mail: pserna@uji.es

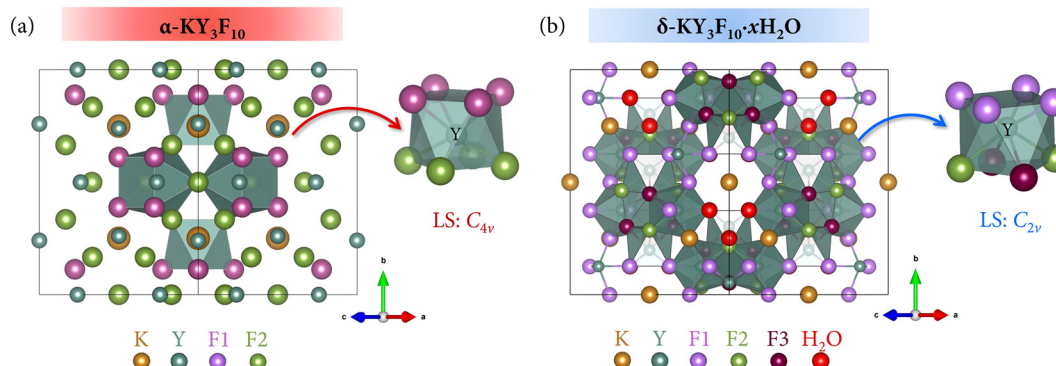† Electronic supplementary information (ESI) available. See DOI: https://doi.org/10.1039/d3ce00614j

Fig. 1 Structure of (a) α-KY$_3$F$_{10}$ and (b) δ-KY$_3$F$_{10}\cdot x$H$_2$O highlighting the coordination polyhedra of Y^{3+} ions along with their local symmetry. The labels F1, F2, and F3 refer to fluoride anions situated at different Wyckoff positions in each compound. The global structure view has been selected for simplification proposes due to the high number of atoms.

While the α-phase has been widely studied in the literature and different synthetic procedures have been developed,[15–19] the obtention of single-phase δ-KY$_3$F$_{10}$ has been more challenging.[20,21] In a recent article, we employed a sonochemical synthesis to obtain both the α and δ compounds by accurately adjusting the pH of the reaction medium.[22] The complex formation mechanism of the δ-phase was discussed in detail employing equilibrium reactions. Inspired by this peculiar and delicate system, we published another study in which a novel and easy coprecipitation method was developed to obtain nanospheres of the δ-phase at room temperature.[21] The results highlighted the delicacy of this fluoride-based system because by only changing the speed of addition of the fluoride source (KF/HF solution) into the Y^{3+} solution it was possible to obtain the single δ-phase or a mixture of $\alpha + \delta$. Additionally, the site-selective emission of the Eu^{3+}-doped δ-phase was found to be 20 times more intense than that of the α-phase, a fact that illustrated the importance of exploring this metastable phase.

Therefore, this last synthesis process was a good candidate to explore the influence of kinetic and thermodynamic factors on the reaction system and the final product. However, as outlined in the ESI† of the present study, it is not possible to properly achieve only the thermodynamic phase (α) by performing several experiments in which the influence of temperature is implemented (thermodynamic conditions). Moreover, another secondary phase starts to appear.

Herein we introduce an enhanced synthetic methodology with some modifications of the coprecipitation strategy previously mentioned that allows to properly follow the transition-phase pathway. To consider both the kinetics and thermodynamics and see how they affect the formation of one or another polymorph, the reaction temperature was varied from 25 to 80 °C, and the reaction time was varied from 1 hour up to 7 days. The results revealed the possibility of isolating both crystal phases depending on the experimental conditions. In addition, due to the different optical responses of both phases, the samples were doped with Eu^{3+}, and all the structural changes were followed by the luminescence of the lanthanide ion.

2. Experimental section

2.1. Materials and methods

The reagents used for the synthesis of the powders were yttrium(III) nitrate hexahydrate [Y(NO$_3$)$_3\cdot$6H$_2$O 99.8%], europium(III) nitrate pentahydrate [Eu(NO$_3$)$_3\cdot$5H$_2$O 99.9%], potassium fluoride [KF 99.5%], and hydrofluoric acid aqueous solution [HF 40% wt]. All of them were purchased from Sigma-Aldrich and used without further purification.

The compounds were prepared by a coprecipitation method. Different temperatures were fixed (25, 40, 60, and 80 °C) combined with different reaction times (1 h, 1 day, and 7 days) yielding a total number of 12 samples. The amounts of reagents were adjusted to obtain approximately 0.5 g of the final product. First, 3.0 mmol of the hydrated Ln(NO$_3$)$_3$ were dissolved in 30 mL of water (0.1 M Ln^{3+} solution; Ln = Y, Eu; 3 mol% Eu^{3+}) in a double-necked round-bottom flask. One of the necks was fitted with a refluxing condenser and the other one was sealed with a rubber septum. The flask was put in a silicon oil bath with the desired temperature fixed. The system was maintained under stirring for 10 min to ensure that the Ln^{3+} solution had achieved the fixed temperature.

After that, the fluoride-source solution was prepared by dissolving 6 mmol of KF in 10 mL of water and, subsequently, adding 270 µL of HF aqueous solution 40% wt. (6 mmol HF). The resulting solution (0.6 M KF/HF) was added dropwise to the previous Ln^{3+} solution in the flask. For that purpose, the rubber septum was removed and it was placed again after finalizing the addition process. Immediately, a white precipitate appeared and it was allowed to mature at the desired time under continuous stirring. Finally, the products were collected by centrifugation, washed twice with water, and dried under an infrared lamp. A summary of the abbreviations used for the samples according to the fixed temperature and reaction time is indicated in Table 1 and a scheme of the experimental procedure is depicted in Fig. 2.

Table 1 Samples prepared under different reaction conditions of time and temperature

T (°C)	1 hour	1 day	7 days
25	R25-1 h	R25-1 d	R25-7 d
40	R40-1 h	R40-1 d	R40-7 d
60	R60-1 h	R60-1 d	R60-7 d
80	R80-1 h	R80-1 d	R80-7 d

2.2. Characterization techniques

Powder X-ray diffraction (XRD) of the samples was performed at room temperature using a Bruker-AX D8-Advance X-ray diffractometer with CuK$_{\alpha 1}$ radiation from $2\theta = 20°$ to 90° at a scan speed of 2.25° min^{-1}. To characterize the morphology of the particles, a JEOL 7001F scanning electron microscope (SEM) was used (acceleration voltage = 30 kV, measuring time = 20 s, and working distance = 8 mm). Previously, the powders had been deposited on double-sided carbon stickers (adhered to the surface of aluminum stubs) and had been sputtered with platinum (10 s).

The photoluminescence response of the materials was recorded with an Eclipse Fluorescence Spectrophotometer (Varian). All the photoluminescence experiments were carried out at room temperature and recorded with a detector delay time (DT) of 0.2 ms to observe the contributions from the higher excited level $^5D_1$ in the emission spectra and discriminate between the optical response of α, δ, and ($\alpha + \delta$) phases. Excitation spectra were recorded in the range 250–500 nm fixing the emission wavelength at 593 nm, while the emission spectra were collected with an excitation at 395 nm in the 500–750 nm range. Time-resolved luminescence measurements were performed at different emission wavelengths (593 nm to collect the $^5D_0 \rightarrow {}^7F_1$ emission and 554 nm to record the response arising from the $^5D_1 \rightarrow {}^7F_2$ transition). The excitation wavelength was monitored at 395 nm ($^7F_0 \rightarrow {}^5L_6$ transition) and lifetime values were extracted from the corresponding decay profiles.

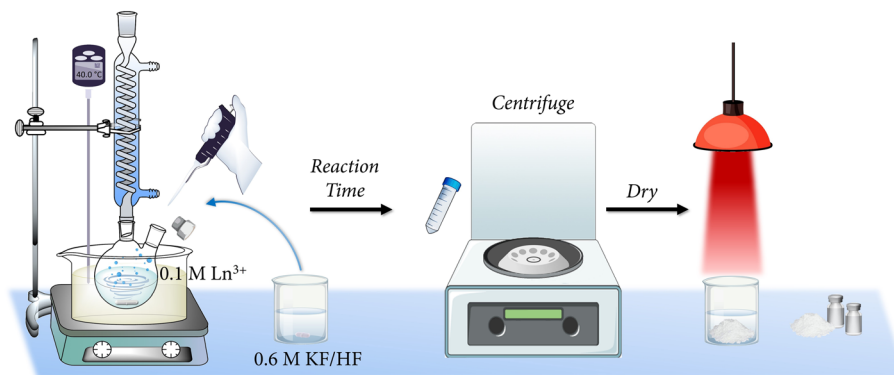## 3. Results and discussion

3.1. Structural characterization

Fig. 3 presents the XRD patterns of the resulting powders under reaction times of (a) 1 h, (b) 1 day, and (c) 7 days. To facilitate the interpretation of the XRD peaks, especially when there is a coexistence of $\alpha + \delta$ phases, the theoretical main reflection peaks for each crystal phase have also been incorporated. The pattern standards used were ICSD card 00-040-9643 (α-KY$_3$F$_{10}$) and ICDD card 04-016-7073 (δ-KY$_3$-F$_{10}$·xH$_2$O). Additionally, Fig. S2 of the ESI† depicts the most useful diffraction peaks that can be used to assign and/or corroborate the presence of the above crystal phases(s).

Regarding Fig. 3(a), with a reaction time of 1 h, it is important to note that at 25 °C a clear mixture of both crystal phases is obtained. This result is optimum to be used as a starting point to study the influence of kinetics and thermodynamics on this particular system. Then, the kinetic factor will be ascribed to the reaction time while the thermodynamic factor, to the reaction temperature. The subsequent increase in the temperature produces a profound effect on the resulting material. The presence of the polymorph δ decreases and only α single-phase is obtained at the maximum temperature of work (80 °C). This tendency evidences the clear importance of the thermodynamic effect to yield the "thermodynamic phase", *i.e.*, α.

Very similar conclusions can be extracted from Fig. 3(b) and (c) if one compares the evolution of the resulting crystal phase(s) with the increase in temperature. However, to analyze the kinetic factor (time) and its influence, one can compare the XRD patterns of samples obtained at the same reaction temperature, but at different maturation times. Perhaps, the most evident and fascinating results are found evaluating the powders obtained at 25 °C. Since the temperature is mild enough to avoid thermodynamic control, it is expected that the kinetic effect becomes more prominent. Indeed, comparing samples R25-1 h, R25-1 d, and R25-7 d, it is clearly shown that the metastable δ-phase is stabilized and R25-7 d contains only this crystal phase without any traces or impurities from α-KY$_3$F$_{10}$. However, it is quite curious that the metastable phase can be stabilized to detriment of the thermodynamic α-phase, as one may expect *a priori*. Further explanations are given below in a subsection.

At 40 °C, the thermodynamic control starts to become slightly more important since the temperature is higher, although not enough to allow the thermodynamics to govern

Fig. 2 Illustrative representation of the experimental procedure followed for the synthesis of the powders.
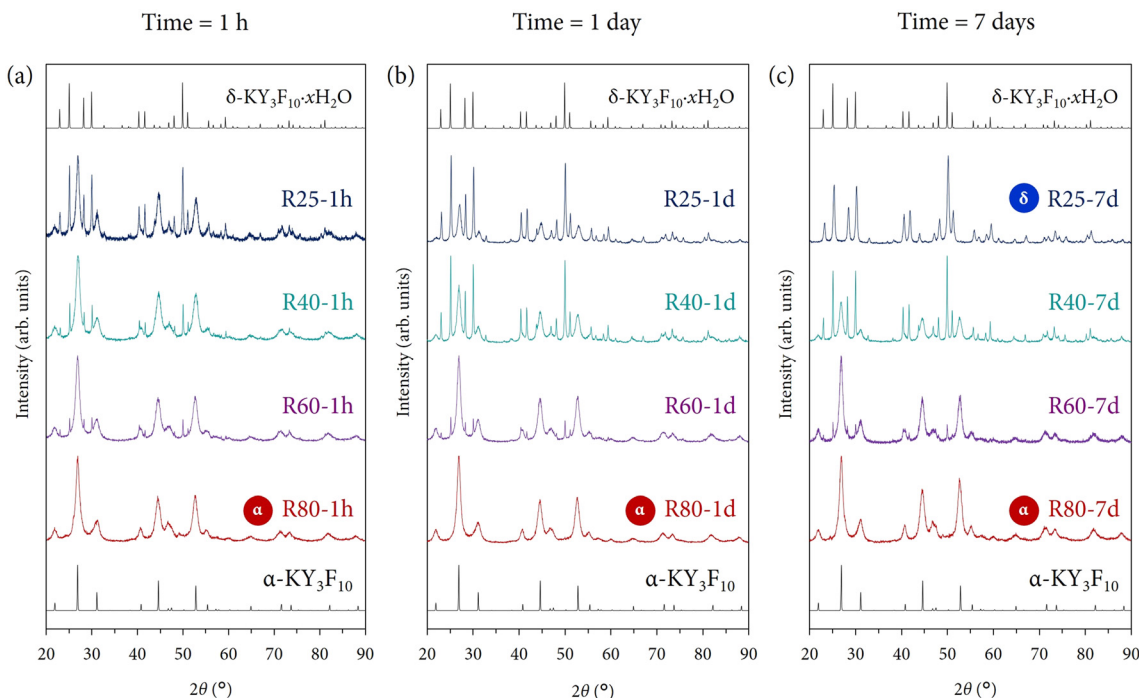
Fig. 3 XRD patterns of the Eu^{3+}-doped powders prepared under different reaction conditions of time and temperature: (a) products prepared with a reaction time of 1 h, (b) products prepared with a reaction time of 1 day, and (c) products prepared with a reaction time of 7 days. For samples that exhibit a single δ-phase (R25-7 d) or single α-phase (R80-1 h, R80-1 d, R80-7 d), the label "α" or "δ" has been added as an inset in the corresponding XRD pattern. The corresponding theoretical ICSD/ICDD cards of the α and δ crystal phases are also shown.

the whole reaction process and neglect the kinetics. The most substantial change occurs between samples R40-1 h and R40-1 d. The XRD pattern corresponding to the latter one presents a higher presence of the metastable δ-phase. This major contribution is even slightly higher at a long reaction time (sample R40-7 d). These results underscore that we are under experimental conditions where the competitiveness between kinetics and thermodynamics plays an important role and it is not possible to obtain either single α or δ-phase.

Following this line of reasoning, when the temperature is increased and set to 60 °C, the thermodynamic control is more than evident because all the XRD patterns of samples R60-1 h, R60-1 d, and R60-7 d exhibit virtually the same profile regardless of the total reaction time. The powders are mainly composed of α-KY_3F_{10} with some minor impurities of δ-KY_3F_{10}, thus highlighting that the kinetics do not play any significant contribution at this point.

This fact is even accentuated considering samples synthesized at 80 °C because independently of the reaction time (1 h, 1 day, or even 7 days), the final product only exhibits the main XRD reflections ascribed to α-KY_3F_{10}. Thereby, thermodynamics governs the whole reaction pathway.

In summary, the structural analysis of the synthesized powders has revealed the possibility of modulating the desired polymorph(s) of KY_3F_{10} thanks to thermodynamic and kinetic control.

Additionally, all the experimental diffraction patterns of the powders were refined using the Rietveld method. The weight fractions (%) of α-KY_3F_{10} and δ-KY_3F_{10} crystal

phases are indicated in Table 2. The values are in very good agreement with the previous discussion of the XRD results and the kinetic/thermodynamic effects. Fig. 4 and 5 depict the Rietveld refinements of the XRD patterns for samples obtained at 25/40 °C, and at 60/80 °C, respectively. Further information about the Rietveld refinement can be found in Section S2 of the ESI.† Table S1 of the ESI† complements the results with the refined unit cell parameter ($a = b = c$) for the different experimental XRD patterns, although no substantial changes seem to take place comparing all the samples.

3.1.1. Understanding the (α + δ) → δ transformation. The Ostwald rule of stages, which is relevant in the study of polymorphism, describes the sequential formation of different crystal structures during crystallization, with less stable phases appearing first and more stable phases following as the process continues.[23] Therefore, one could expect that when exposing sample R25-1 h (α + δ) to long maturing times (R25-7 d, 7 days of maturation), the product

Table 2 Weight fractions (%) of α-KY_3F_{10} and δ-$KY_3F_{10}\cdot xH_2O$ crystal phases obtained using the Rietveld refinement of the different XRD patterns of the powders

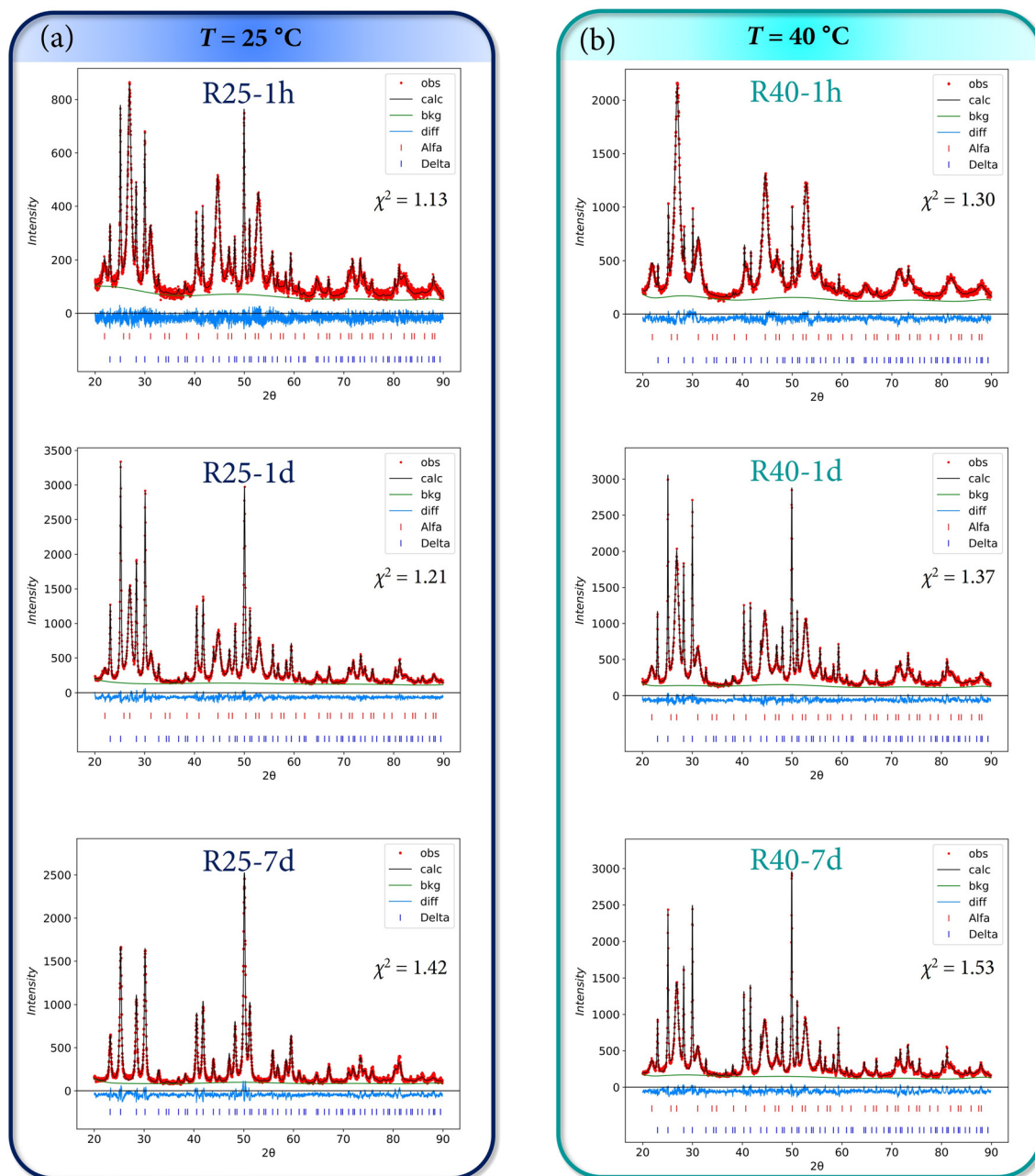| T (°C)	% α			% δ		
	1 hour	1 day	7 days	1 hour	1 day	7 days
25	68.3	41.9	0	31.7	58.1	100
40	92.8	63.7	61.3	7.2	36.3	38.7
60	95.1	93.9	93.6	4.9	6.1	6.4
80	100	100	100	0	0	0

Fig. 4 Rietveld refinements of the XRD patterns for samples obtained at (a) 25 °C and (b) 40 °C. The goodness of fit χ^2 parameter is also indicated in each plot.

would evolve toward the formation of the most thermodynamic polymorph, which in this case is α-KY_3F_{10}. Surprisingly, the opposite behavior occurs, being able to isolate the δ-phase in sample R25-7 d.

To shed some light on the mechanism underlying such crystal phase transformation, further experiments were conducted to prove whether it would be possible, or not, for α to dissociate into the corresponding ions in the reaction medium and then form the less stable δ-phase. For that purpose, the pure α-KY_3F_{10} was synthesized following the same experimental conditions as those described for sample R80-1 h ($T = 80$ °C, reaction time = 1 hour). Then, the resulting

precipitate in the reaction medium was allowed to cool down until room temperature under continuous stirring. To have a better understanding of the process of transformation, several aliquots of the mixture were taken during one week. The dried powders were characterized by XRD diffraction and the results showed that the sample did not experience any partial α to δ phase transformation (see Fig. S3 of the ESI†).

Although this fact seems to be somewhat counterintuitive, there are several studies in the literature that address the crystallization of polymorphs that do not follow Ostwald's rule of stages.[24–26] Quite often, a process can result in the simultaneous crystallization of multiple polymorphic
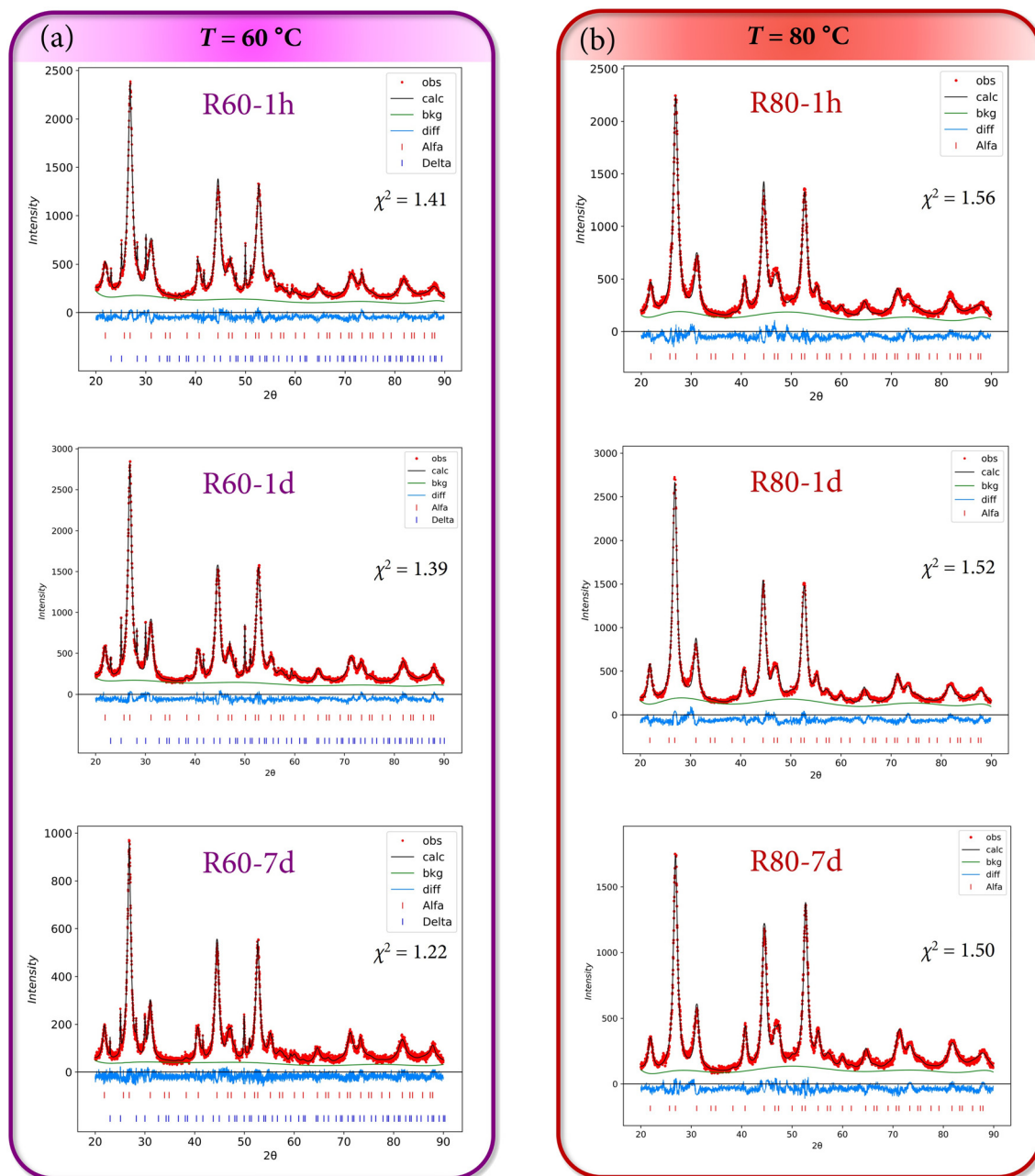
Fig. 5 Rietveld refinements of the XRD patterns for samples obtained at (a) 60 °C and (b) 80 °C. The goodness of fit χ^2 parameter is also indicated in each plot.

structures, further complicating the control of polymorphism, as is our case (*e.g.* sample R25-1 h). Various mechanisms have been suggested to explain this occurrence, which is referred to as concomitant polymorphism. This phenomenon has been attributed to competing processes of nucleation that can lead to the cross-nucleation of a metastable polymorph on the stable polymorph and finally obtain the less stable polymorph.[27] Therefore, the observed results could indicate that the α to δ phase transformation might undergone a cross-nucleation mechanism, as depicted schematically in Fig. 6.

Following this line of reasoning, the formation of crystal nuclei consisting of α particles would take place first and

fast. Then, nuclei of δ particles would start to crystallize on the surfaces of the most stable α-nuclei. Subsequently, the amount of δ-phase would start to become more prominent until finally this polymorph is isolated despite being less stable thermodynamically. We believe that these interesting results should be subjected to further study and confirmed with future lines of research.

3.2. Morphological characterization

Given the structural results, it is of interest to analyze the morphology of the particles in order to illustrate their
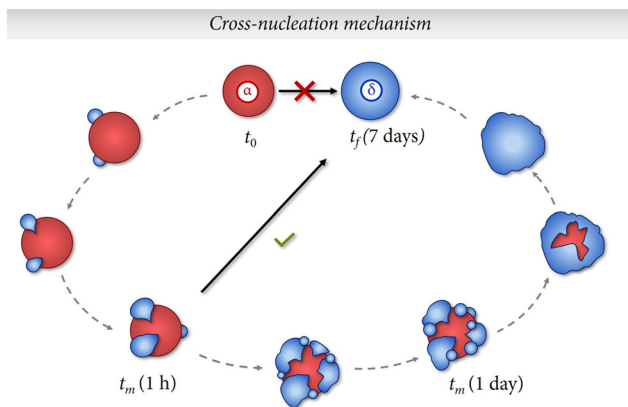
Fig. 6 Schematic representation of the suggested cross-nucleation mechanism that explains the obtention of the metastable δ-phase instead of the thermodynamic α-phase when exposing the precipitate (α + δ) at long times of maturing. t_m indicates an intermediate time of maturing.

evolution and corroborate the kinetic/thermodynamic effects. Fig. 7 presents the SEM images of the Eu^{3+}-doped powders prepared under different reaction conditions of time and temperature.

Fig. 7(a) shows the micrographs of samples synthesized at 25 °C with different maturing times. Sample R25-1 h is mainly composed of particle aggregates without a morphology clearly defined. Notwithstanding, with the evolution of time, the aggregates tend to form spherical particles, with the most notable effect appreciated in sample R25-7 d (single δ-phase), in which the coalescence of spheres is demonstrated. Thus, not only does the kinetics serve as a director of the crystal structure but also as a morphological modulator.

Regarding Fig. 7(b), *i.e.*, samples synthesized at 40 °C, no substantial changes can be appreciated depending on the reaction time. However, a major degree of order (particles with more regular shapes instead of large aggregates) is formed at this temperature. Compare for instance sample R40-1 h with R25-1 h.

In a similar way to the results issued by the XRD analysis, where no difference was appreciated among the samples at different reaction times, the SEM images of Fig. 7(c) corresponding to powders obtained at 60 °C reflect the same
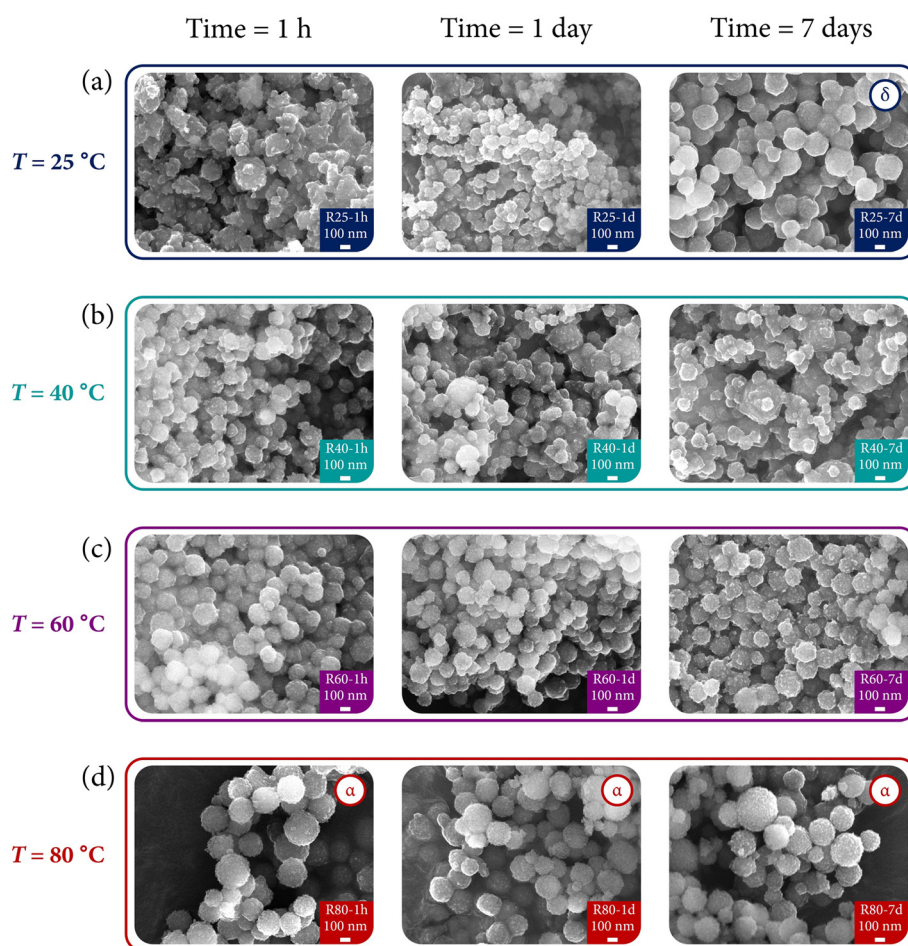

Fig. 7 SEM images of the Eu^{3+}-doped powders prepared under different reaction conditions of time and temperature: (a) compounds prepared at 25 °C, (b) compounds prepared at 40 °C, (c) compounds prepared at 60 °C, and (d) compounds prepared at 80 °C. For samples that exhibit a single δ-phase (R25-7 d) or single α-phase (R80-1 h, R80-1 d, R80-7 d), the label "α" or "δ" has been added as an inset in the corresponding micrograph.
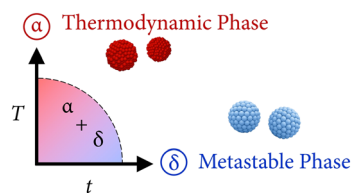
Fig. 8 Schematic representation of the influence of the thermodynamic (temperature) and kinetic (time) factors that allow to obtain both crystal phases.

Fig. 9 Room temperature excitation spectra obtained with a DT = 0.2 ms for different samples as an example of the δ-phase, α-phase, and α + δ. The dashed line at 395 nm serves as a guideline to observe that there are no substantial changes in the excitation spectra of the different powders and the maximum intensity corresponds to the band associated with the $^7F_0 \rightarrow {}^5L_6$ transition (395 nm).

behavior. As previously commented with samples of Fig. 7(b), the temperature (and, thus the thermodynamic factor) also contributes to the formation of more regular sphere-shaped particles.

Finally, Fig. 7(d) underscores two main points: (1) the good correlation between the structural and morphological characterization, and (2) the prevalence of the thermodynamic control over the particle shapes. Interestingly, all the powders (which present the α-KY$_3$F$_{10}$ polymorph) exhibit the same morphology regardless of the reaction time: spherical particles resulted from the self-assembly of subunits around 20 nm. More intriguing is the fact that this morphology is the same that has been possible to obtain under the aforementioned process of synthesis mediated by sonochemistry.[22]

Hence, the evolution of the polymorphs is governed by kinetic and/or thermodynamic control, also reflected in the evolution of the morphology of particles. As a schematic representation, Fig. 8 summarizes the above effects. At the beginning (sample R25-1 h), a mixture of both α and δ phases is obtained, but with the incorporation of the thermodynamic (temperature) or kinetic (time) factors it is possible to modulate the formation of a single crystal phase.

3.3. Photoluminescence properties

3.3.1. Excitation and emission spectra. One of the main key points of this study is the capability of relating the luminescent response of the materials with the thermodynamic and/or the kinetic effect throughout the reaction pathway. Thus, a direct measurement, as it is the luminescence of the Eu^{3+}-doped powders, serves to easily interpret the structure–stability conjunction because the two polymorphs of interest exhibit some particular differences regarding the optical response.

Fig. 9 shows the room temperature excitation spectra for different samples as an example of the δ-phase (R25-7 d), α-phase (R80-1 h), and α + δ (R25-1 h). Regardless of the sample composition, there are no substantial changes in the excitation spectra of the different powders. All the bands can be attributed to the transitions of Eu^{3+} from the ground $^7F_0$ level to higher excited levels. As outlined with the dashed line, the maximum intensity corresponds to the band associated with the $^7F_0 \rightarrow {}^5L_6$ transition (395 nm).
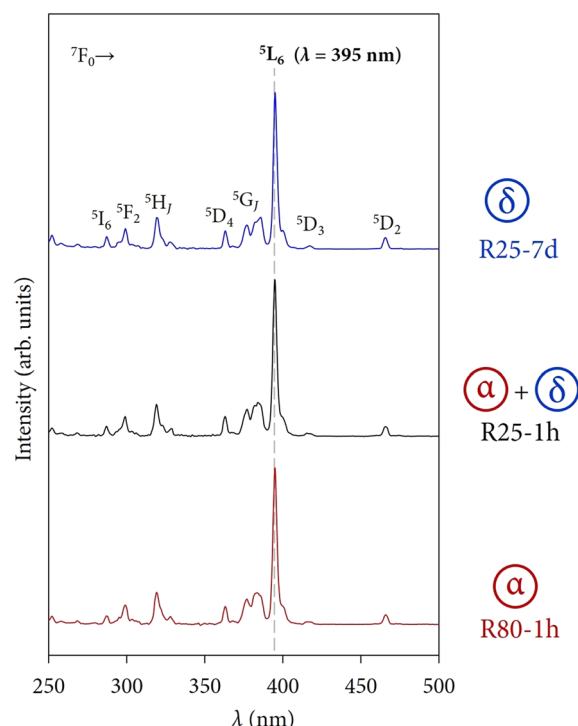
In addition, there are no bands associated with charge transfers (CTs) from the anions of the host lattice (F$^-$) to the Eu^{3+} ion. For Eu^{3+}-doped fluorides, the F$^-$–Eu^{3+} CT appears at high-energy positions in comparison with oxidic matrices because of the band gap of compounds and the optical electronegativity of the ions implied.[28–30] These CTs usually have low intensity and are expected to appear in the 150–170 nm spectral region so they might be difficult to detect sometimes due to instrumental limitations.[31] Therefore, the emission spectra of the powders have been recorded under an excitation wavelength of 395 nm.

Regarding the emission profiles of the powders, Fig. 10 depicts a selection of four spectra as an example to appreciate at first glance the modulation and changes in the photoluminescence response of the compounds depending on the polymorph(s). The observed bands correspond to the common $^5D_0 \rightarrow {}^7F_J$ transitions of Eu^{3+} but, due to the different electronic nature of the α and δ phases, the presence of bands associated with transitions arising from the higher excited state $^5D_1$ can also be observed (marked with black stars in Fig. 10).[32] The presence of transitions from higher excited states is attributed to the typical low phonon energies of fluorides (300–550 cm^{-1}).[33,34] The internal vibrations of the host lattice are low enough to avoid fast and non-radiative multiphonon relaxation processes from the $^5L_6$ state to the lowest-lying excited state $^5D_0$, allowing the observation of such $^5D_1 \rightarrow {}^7F_J$ emissions.[35,36]
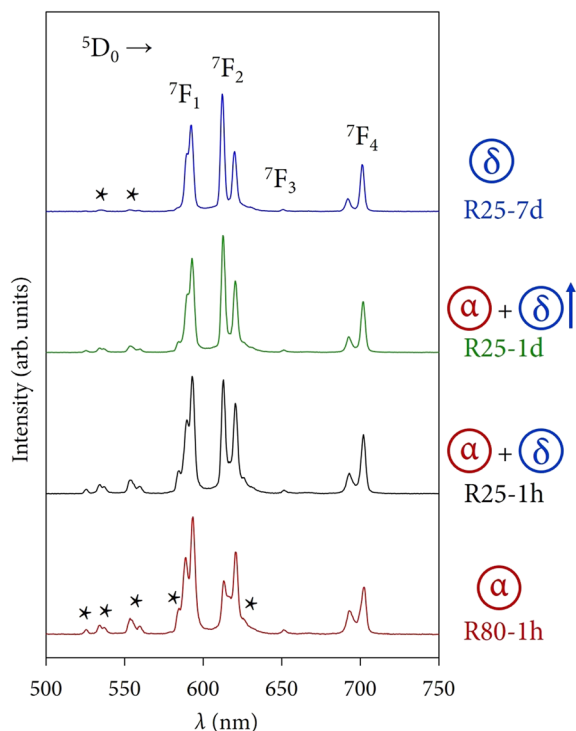
Fig. 10 Room temperature emission spectra obtained with a DT = 0.2 ms for different samples where the modulation of the crystal phases is reflected in the optical response. The stars in the emission spectra indicate bands associated with $^5D_1 \rightarrow {}^7F_J$ transitions from the higher excited state $^5D_1$.

Sample R80-1 h (α) is dominated by the $^5D_0 \rightarrow {}^7F_1$ magnetic dipole transition, whose main peak appears at 395 nm. Samples R25-1 h ($\alpha + \delta$) and R25-1 d ($\alpha + \delta$, with a major contribution of the δ-phase) exhibit an intermediate optical response between the two crystal phases. It can be well appreciated how the peaks corresponding to the $^5D_1 \rightarrow {}^7F_J$ transitions start to almost disappear and the $^5D_0 \rightarrow {}^7F_2$ electric dipole transition (with the most intense peak at 621 nm) becomes more prominent. Finally, the photoluminescence of sample R25-7 d (δ) is governed by the $^5D_0 \rightarrow {}^7F_2$ transition and the $^5D_1 \rightarrow {}^7F_J$ emissions are still present, albeit with very low intensity, a fact that will be directly related to the lifetimes of these states in the next section.

3.3.2. The crystal environment of Eu^{3+} ions. In contrast to other rare earth (RE) ions, the distinctive attributes intrinsic to the electronic configuration of Eu^{3+} render this trivalent ion particularly esteemed within the realm of photoluminescence,

especially due to its ability to act as a site-sensitive structural probe.[37,38] This unique characteristic engenders a significant advantage, as it facilitates the extraction of pivotal insights regarding the crystal field surroundings of europium ions that have been incorporated into a host lattice. The analysis of the emission spectrum, therefore, emerges as a powerful and informative tool for elucidating the intricacies of the host matrix and its interaction with Eu^{3+} ions, which is of the utmost interest in this case since the optical response and associated physicochemical parameters are expected to be different for both α and δ crystal phases.

The great advantage is that these physicochemical parameters (such as the well-known asymmetry ratio R, or the Judd Ofelt parameters) can be directly extracted from the emission spectra, a fact that allows for the avoidance of many complex mathematical and computational calculations, as it is the case in other rare earth ions.

Probably, the most popular parameter of Eu^{3+} is the asymmetry ratio, which can be calculated from the ratio between the integrated intensities of the $^5D_0 \rightarrow {}^7F_2$ electric dipole (ED) and $^5D_0 \rightarrow {}^7F_1$ magnetic dipole (MD) transitions. This ED transition has a hypersensitive character to the ion's environment, while the intensity of the above MD transition is relatively independent of the Eu^{3+} symmetry for a given material. Thereby, R provides some useful information about the local symmetry of the luminescent ion.

In direct connection with the structural analysis from the emission spectrum of the luminescent centers, the Judd Ofelt (JO) theory and the corresponding parameters emerge as a robust framework for understanding and predicting the optical properties of rare earth ions. The Ω_2 parameter is linked to the polarizability and covalent nature of the RE^{3+} ion, offering valuable insights into the surrounding crystal structure of Eu^{3+}. Consequently, it is regarded as a parameter that primarily reflects the local environment.[39] In fact, $\Omega_2 \propto R$ for the europium ions of the material under consideration.[40] Hence, larger values of R and Ω_2 tend to indicate lower symmetry of Eu^{3+} ions in the host lattice.[41,42] On the other hand, Ω_4 is known as the long-range JO parameter because it is sensitive to macroscopic properties such as viscosity and rigidity.[43]

The above parameters can be calculated by making use of some physical equations,[44,45] although recent application software packages incorporate them and highly facilitate the calculus.[46,47] The JO and R parameters were calculated using the LUMPAC software package and are presented in Table 3. It must be noted that these parameters refer exclusively to

Table 3 Asymmetry ratio (R) values and Judd–Ofelt parameters (Ω_2, Ω_4) for the Eu^{3+}-doped powders synthesized at different temperatures and reaction times

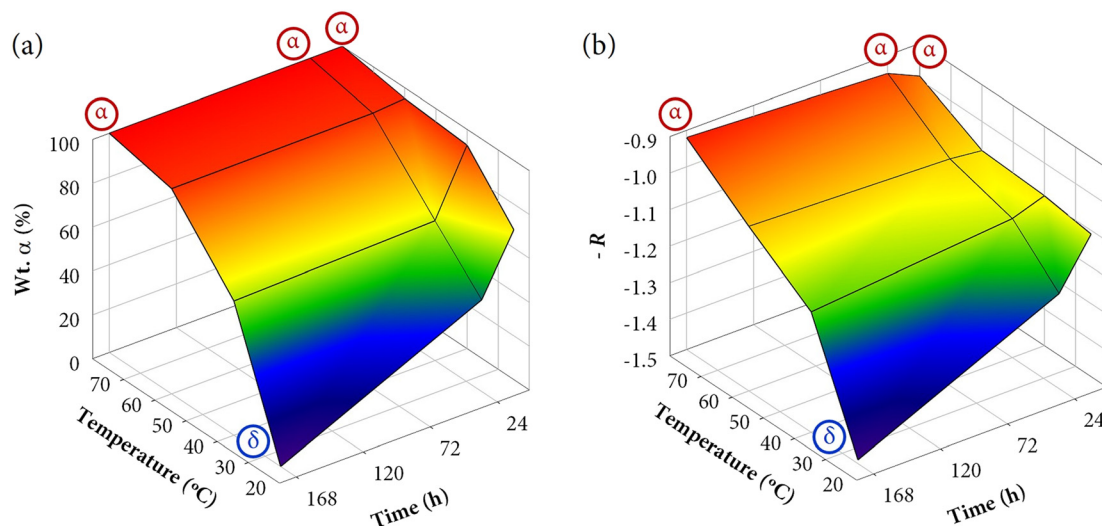| T (°C)	R			Ω_2 (10^{-20} cm^2)			Ω_4 (10^{-20} cm^2)		
	1 hour	1 day	7 days	1 hour	1 day	7 days	1 hour	1 day	7 days
25	1.11	1.24	1.49	2.02	2.19	2.62	1.87	1.90	1.99
40	1.09	1.12	1.17	1.89	1.99	2.08	1.87	1.99	1.94
60	1.08	1.07	1.05	1.97	1.94	1.88	2.04	2.00	1.91
80	0.99	0.95	0.92	1.82	1.78	1.69	1.86	1.89	1.92

Fig. 11 3D plots of (a) the weight fractions of α-KY$_3$F$_{10}$ and (b) the negation of the asymmetry ratio as a function of temperature and time. For samples that exhibit a single δ-phase (R25-7 d) or single α-phase (R80-1 h, R80-1 d, R80-7 d), the label "α" or "δ" has been added as an inset in the corresponding point.

the $^5D_0 \rightarrow {}^7F_J$ transitions. Therefore, to accurately calculate them, they were extracted from the emission spectra of the samples that were recorded again setting a detector delay time (DT) of 10 ms, which ensures the avoidance of contribution from the higher excited state $^5D_1$.[34] An example of the emission spectrum at different DTs is presented in Fig. S4 of the ESI.†

As mentioned, $\Omega_2 \propto R$, therefore, the discussion of the obtained results will be addressed for the asymmetry ratio (the same conclusions can be extracted from the analysis of Ω_2). Theoretically, the Eu^{3+} ions occupying the yttrium positions in the α phase would have an ideal C_{4v} local symmetry, while it would be C_{2v} for Eu^{3+} ions incorporated into the δ phase. As a result, it is expected to obtain, *a priori*, lower values of R (more symmetric sites) for samples containing major fractions of the α phase.

The analysis of the results presented in Table 3 confirms this hypothesis. The evolution of the α/δ content was more remarkable in samples synthesized at 25 and 40 °C. For example, the weight fractions of α phase in samples R25-1 h (68.3%), R25-1 d (41.9%), and R25-7 d (0%) are directly related to the occupation of C_{2v} sites in a major proportion, as reflected in the increase of the asymmetry ratio values: R25-1 h (1.11), R25-1 d (1.24), and R25-7 d (1.49). To appreciate at first glance the correlation between the weight fractions and R, 3D plots (fraction-time–temperature and asymmetry-time–temperature) are depicted in Fig. 11. For visual purposes, instead of plotting the R values, it has been plotted the negation of the asymmetry ratio (*i.e.*, $-R$). Thus, higher values of $-R$ indicate more symmetry in the crystal environment of Eu^{3+} ions (more fraction of α phase).

On the other hand, it must be recalled that the Ω_4 JO parameter is ascribed to bulk properties. For this reason, due to the wide range of morphologies observed and other macroscopic properties that can present the materials, it is

complicated to establish a direct relationship among the different series of samples.

3.3.3. Time-resolved luminescence. The lifetimes associated with a specific electronic transition can serve as a probe to check structural/local distortions,[48,49] and phase transformations between different polymorphs.[50,51] Therefore, lifetimes are of the utmost interest to follow the changes produced in the synthesized powders by kinetic and thermodynamic effects during the reaction pathway.

Herein, taking advantage of the presence of $^5D_1 \rightarrow {}^7F_J$ transitions, it is possible to measure the lifetimes of the materials for different excited states ($^5D_0$ and $^5D_1$) since their sensitivity to the structural changes might be different. Thus, it is pretended to extract more information about the photoluminescence properties of the compounds and check to what extent such an inherent relationship can be established.

In direct connection with the emission results previously discussed, Fig. 12 displays the decay curves of some selected samples (the same used in Fig. 10). For the $^5D_0$ state, Fig. 12(a), the emission was collected at 593 nm ($^5D_0 \rightarrow {}^7F_1$ transition), while for the $^5D_1$, Fig. 12(b), it was collected at 554 nm ($^5D_1 \rightarrow {}^7F_2$ transition). At first glance, it can be observed that the decay profiles change during the phase transformation. In both cases, the red (R80-1 h, α) and blue curves (R25-7 d, δ) are very different. The decay curves were best fitted to a double exponential model ($R^2 \geq 0.999$) following the expression:

$$I(t) = I_1 \exp\left(\frac{-t}{\tau_{obs1}}\right) + I_2 \exp\left(\frac{-t}{\tau_{obs2}}\right) \tag{1}$$

where I refers to the intensity as a function of time (t). To easily compare the results, an effective lifetime (τ_{eff}), presented in Table 4, was calculated according to:
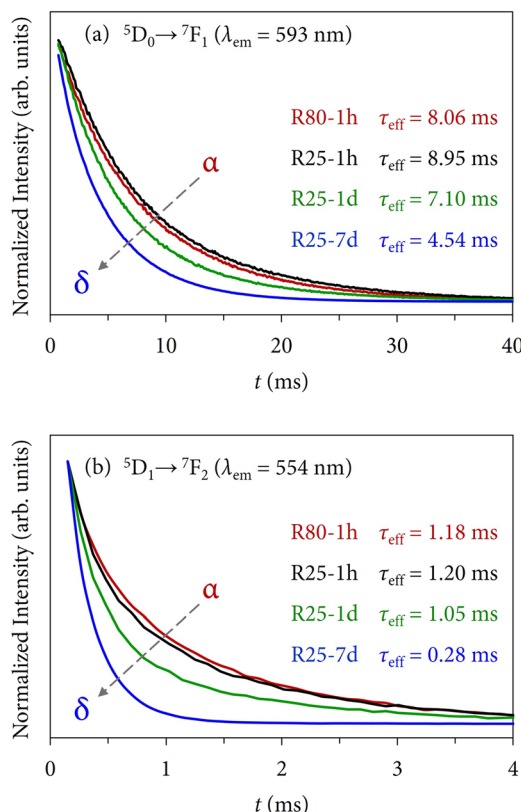
Fig. 12 Normalized decay curves acquired at room temperature with a DT = 0.2 ms exciting the samples at 395 nm and collecting the emission at (a) 593 nm ($^5D_0 \rightarrow {}^7F_1$ transition) for the lowest-lying excited state $^5D_0$, and (b) 554 nm ($^5D_1 \rightarrow {}^7F_2$ transition) for the higher excited state $^5D_1$.

$$\tau_{eff} = \frac{I_1(\tau_{obs1})^2 + I_2(\tau_{obs2})^2}{I_1(\tau_{obs1}) + I_2(\tau_{obs2})} \qquad (2)$$

The results indicate that the lifetimes corresponding to the $^5D_1$ state are shorter than those of the $^5D_0$, a phenomenon strictly linked to the cross-relaxation process in which Eu^{3+} ions populating the higher excited level decay to the metastable $^5D_0$.[52] Further information about the fitting procedure can be found in Section S4 of the ESI.†

First, the $^5D_0$ lifetimes will be analyzed, which are also in good agreement with the XRD and SEM results. Samples

Table 4 $^5D_0$ and $^5D_1$ lifetimes calculated from the corresponding decay profiles of the samples. All the correlation coefficients of the fits (R^2) were ≥0.999

T (°C)	τ_{eff} $^5D_0 \rightarrow {}^7F_1$ (ms)			τ_{eff} $^5D_1 \rightarrow {}^7F_2$ (ms)		
	1 hour	1 day	7 days	1 hour	1 day	7 days
25	8.95(6)	7.10(4)	4.54(1)	1.20(3)	1.05(3)	0.28(4)
40	8.72(4)	7.87(3)	7.49(3)	1.15(2)	1.09(3)	1.03(2)
60	8.63(4)	9.15(1)	9.25(5)	1.17(3)	1.23(2)	1.22(2)
80	8.06(3)	8.37(1)	8.68(4)	1.18(2)	1.20(2)	1.23(2)

synthesized at 25 °C display a progressive shortening of the lifetimes (from 8.95 ms of the α + δ mixture to 4.54 ms of single δ). Similarly, samples obtained at 40 °C also exhibit shorter lifetimes with the evolution of time, which can be well ascribed to the major presence of the δ-phase. On the other hand, although the XRD results showed that the crystal structure composition of samples synthesized at 60 °C (mainly α + some minor contribution of δ) and at 80 °C (α) was constant regardless of the maturing time because the thermodynamic control governed the reaction pathways, there is a tendency in the lifetimes to become longer as the reaction time increases, which is the opposite trend in comparison with the above series of samples. *A priori*, one could think that this fact could be associated with morphological aspects, however, the micrographs outlined that there were no substantial changes among each series of samples. Therefore, the main possible explanation could be associated with a local rearrangement or ordering of Eu^{3+} ions when the precipitate is exposed to high reaction times that allow for a more uniform distribution of the dopant in the crystal lattice, as might be inferred from the asymmetry ratio and the Ω_2 JO parameter, see Table 3. Thus, even though the thermodynamics govern the crystallization of the compound in the latter samples, the kinetics (maturation time) has also some particular influence.

Moreover, it is interesting to note that when both polymorphs coexist in the sample, slightly longer lifetimes are obtained. The most evident examples can be found comparing samples synthesized in 1 h at different temperatures: the τ_{eff} shortens progressively from 8.95 ms (R25-1 h) to 8.06 ms (R80-1 h). This behavior has also been reported previously[21] and might be related to different coupling mechanisms between Eu^{3+} ions embedded in the different host lattices that, as a result, tend to elongate the lifetime.

On the other hand, regarding the lifetimes associated with the $^5D_1$ state, similar conclusions can be drawn. However, the optical response of the $^5D_1 \rightarrow {}^7F_J$ transitions is primarily attributed to the presence of Eu^{3+} ions in α-KY_3F_{10} with an almost negligible contribution of the dopant in δ-KY_3F_{10} (as depicted in Fig. 10 for sample R25-7 d). Therefore, the variation of the $^5D_1$ lifetime values in the different series of samples is less notable ($\tau_{eff} \approx$ 1.0–1.2 ms) in comparison to the $^5D_0$ lifetimes. Remarkably, a drastic change is observed for sample R25-7 d (δ-KY_3F_{10}) whose lifetime is 0.28 ms.

Additionally, 3D plots (lifetime-time–temperature) are depicted in Fig. 13 to compare the kinetic and thermodynamic effects on the resulting lifetimes. As can be appreciated, both graphics evince the perfect relationship and good agreement with the tendency observed in the results previously discussed. The color gradient is very useful to easily interpret the changes. Moreover, they closely resemble the 3D plots of Fig. 11 (weight fractions of α-KY_3F_{10} and asymmetry ratio R).
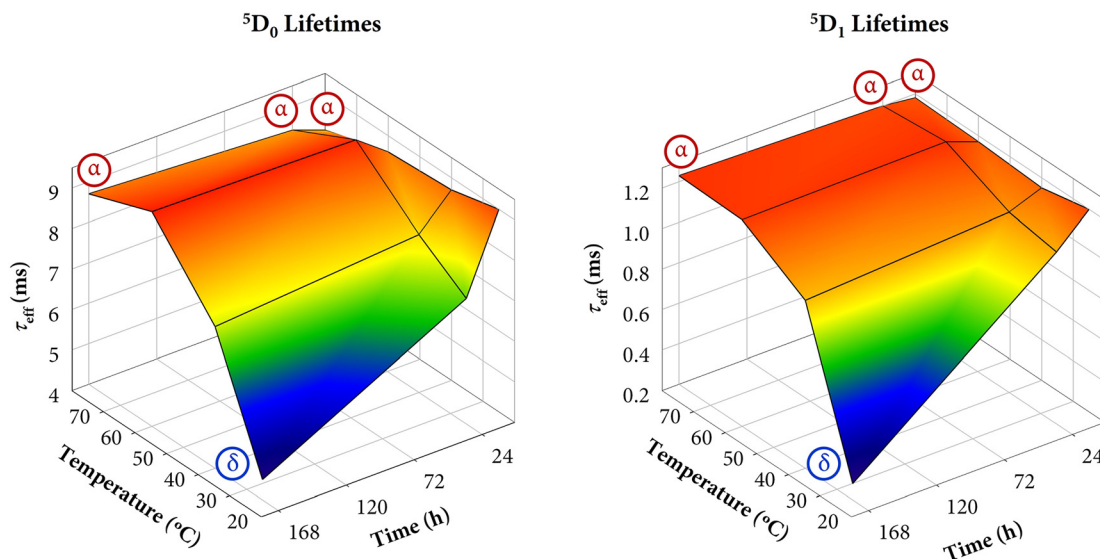
Fig. 13 3D plot of the lifetimes corresponding to the $^5D_0$ and $^5D_1$ states as a function of temperature and time. For samples that exhibit a single δ-phase (R25-7 d) or single α-phase (R80-1 h, R80-1 d, R80-7 d), the label "α" or "δ" has been added as an inset in the corresponding point.

4. Conclusions

To control and follow the transition-phase pathway of the two existent polymorphs of KY_3F_{10} (α and δ), an enhanced coprecipitation strategy has been used to synthesize different Eu^{3+}-doped powders, which contain a mixture of both crystal phases in different proportions or single-phases. The kinetics and thermodynamics effects have been able to study varying reaction conditions of temperature (25–80 °C) and time (1 hour to 7 days).

The results underscored the competitiveness between kinetics and thermodynamics. At low reaction temperature (25 °C), it is possible to modulate the crystal structure with the maturing time and the metastable δ-phase can be isolated after 7 days. However, when the temperature starts to increase (40 °C) the thermodynamic control becomes more prominent. Although the kinetics still play an important role and an evolution toward the formation of the δ-phase is evident with the reaction time, it is no longer possible to isolate this compound and only a mixture of polymorphs is obtained. Finally, higher working temperatures change dramatically the system and evidence the total thermodynamic control of the reaction pathway. Indeed, the α polymorph is always obtained at 80 °C regardless of the maturing time.

The microstructural analysis of the powders matches very well with the above structural results, being able to observe the influence of thermodynamics and kinetics in the particle morphology.

Finally, bearing in mind the good adequacy of the Eu^{3+} ion to act as a sensitive structural probe, the optical response of the prepared materials is in direct connection with the presence of one or both polymorphs and thus it serves as a perfect tool to control the kinetics and thermodynamics effects in the reaction pathway.

Author contributions

P. Serna Gallén: conceptualization, methodology, investigation, writing (original draft, review & editing). E. Cordoncillo and H. Beltrán-Mir: conceptualization, funding acquisition, writing (review & editing).

Conflicts of interest

There are no conflicts to declare.

Acknowledgements

References

1 M. Bianchini, J. Wang, R. J. Clément, B. Ouyang, P. Xiao, D. Kitchaev, T. Shi, Y. Zhang, Y. Wang, H. Kim, M. Zhang, J. Bai, F. Wang, W. Sun and G. Ceder, The interplay between thermodynamics and kinetics in the solid-state synthesis of layered oxides, *Nat. Mater.*, 2020, **19**, 1088–1095, DOI: **10.1038/s41563-020-0688-6**.

2 B. Hu, S. Sridar, L. Hao and W. Xiong, A new thermodynamic modeling of the Ti–V system including the metastable ω phase, *Intermetallics*, 2020, **122**, 106791, DOI: **10.1016/j.intermet.2020.106791**.

3 D. Rabadjieva, K. Sezanova, R. Gergulova, R. Titorenkova and S. Tepavitcharova, Precipitation and phase transformation of dicalcium phosphate dihydrate in electrolyte solutions of simulated body fluids: Thermodynamic modeling and kinetic

studies, *J. Biomed. Mater. Res., Part A*, 2020, **108**, 1607–1616, DOI: **10.1002/jbm.a.36929**.

4 Q. Luo, Y. Guo, B. Liu, Y. Feng, J. Zhang, Q. Li and K. Chou, Thermodynamics and kinetics of phase transformation in rare earth–magnesium alloys: A critical review, *J. Mater. Sci. Technol.*, 2020, **44**, 171–190, DOI: **10.1016/j.jmst.2020.01.022**.

5 T. Wang, Q. Fan and J. Zhu, Steering On-Surface Reactions by Kinetic and Thermodynamic Strategies, *J. Phys. Chem. Lett.*, 2023, **14**, 2251–2262, DOI: **10.1021/acs.jpclett.3c00001**.

6 V. V. Gostishchev, I. A. Astapov, A. V. Seredyuk, S. N. Khimukhin and R. Hosen, High-temperature synthesis of composites based on nickel aluminides, *Inorg. Mater.*, 2016, **52**, 419–422, DOI: **10.1134/S0020168516040051**.

7 X. Gong, H. Noh, N. C. Gianneschi and O. K. Farha, Interrogating Kinetic versus Thermodynamic Topologies of Metal-Organic Frameworks via Combined Transmission Electron Microscopy and X-ray Diffraction Analysis, *J. Am. Chem. Soc.*, 2019, **141**, 6146–6151, DOI: **10.1021/jacs.9b01789**.

8 H. Liu, J. Han, C. McBean, C. S. Lewis, P. Kumar Routh, M. Cotlet and S. S. Wong, Synthesis-driven, structure-dependent optical behavior in phase-tunable NaYF₄:Yb,Er-based motifs and associated heterostructures, *Phys. Chem. Chem. Phys.*, 2017, **19**, 2153–2167, DOI: **10.1039/c6cp07648c**.

9 B. Shao, Q. Zhao, Y. Jia, W. Lv, M. Jiao, W. Lü and H. You, A novel synthetic route towards monodisperse β-NaYF₄:Ln³⁺ micro/nanocrystals from layered rare-earth hydroxides at ultra low temperature, *Chem. Commun.*, 2014, **50**, 12706–12709, DOI: **10.1039/c4cc05191b**.

10 D. Gentili, M. Gazzano, M. Melucci, D. Jones and M. Cavallini, Polymorphism as an additional functionality of materials for technological applications at surfaces and interfaces, *Chem. Soc. Rev.*, 2019, **48**, 2502–2517, DOI: **10.1039/c8cs00283e**.

11 R. Alvarez-Roca, A. F. Gouveia, C. C. De Foggi, P. S. Lemos, L. Gracia, L. F. Da Silva, C. E. Vergani, M. San-Miguel, E. Longo and J. Andrés, Selective Synthesis of α-, β-, and γ-Ag₂WO₄ Polymorphs: Promising Platforms for Photocatalytic and Antibacterial Materials, *Inorg. Chem.*, 2021, **60**, 1062–1079, DOI: **10.1021/acs.inorgchem.0c03186**.

12 KY₃F₁₀ Crystal Structure: Datasheet from PAULING FILE Multinaries Edition – 2012 in Springer Materials, ed. P. Villars and K. Cenzual, (**https://materials.springer.com/isp/crystallographic/docs/sd_0552093**).

13 δ-KY₃F₁₀·xH₂O (KY₃F₁₀[H₂O]) Crystal Structure: Datasheet from "PAULING FILE Multinaries Edition – 2012" in Springer Materials, ed. P. Villars and K. Cenzual, (**https://materials.springer.com/isp/crystallographic/docs/sd_1004004**).

14 F. Le Berre, E. Boucher, M. Allain and G. Courbion, Synthesis, stability and zeolitic behavior of δ-ALn₃F₁₀,xH₂O and γ-ThLn₂F₁₀,H₂O phases (Ln=lanthanide), *J. Mater. Chem.*, 2000, **10**, 2578–2586, DOI: **10.1039/b002520h**.

15 L. Zhu, J. Meng and X. Cao, Sonochemical synthesis of monodispersed KY₃F₁₀:Eu³⁺ nanospheres with bimodal size

distribution, *Mater. Lett.*, 2008, **62**, 3007–3009, DOI: **10.1016/j.matlet.2008.01.096**.

16 C. Cao, Hydrothermal synthesis, phase evolution, and optical properties of Eu³⁺-doped KF-YF₃ system materials, *J. Mater. Res. Soc.*, 2012, **27**, 2988–2995, DOI: **10.1557/jmr.2012.331**.

17 S. Goderski, M. Runowski and S. Lis, Synthesis of luminescent KY₃F₁₀ nanopowder multi-doped with lanthanide ions by a co-precipitation method, *J. Rare Earths*, 2016, **34**, 808–813, DOI: **10.1016/S1002-0721(16)60098-4**.

18 M. Runowski, Color-tunable up-conversion emission of luminescent-plasmonic, core/shell nanomaterials-KY₃F₁₀: Yb³⁺,Tm³⁺/SiO₂-NH₂/Au, *J. Lumin.*, 2017, **186**, 199–204, DOI: **10.1016/j.jlumin.2017.02.032**.

19 M. Chen, P. Loiko, J. M. Serres, S. Veronesi, M. Tonelli, M. Aguiló, F. Díaz, S. Y. Choi, J. E. Bae, F. Rotermund, S. Dai, Z. Chen, U. Griebner, V. Petrov and X. Mateos, Fluorite-type Tm³⁺:KY₃F₁₀: A promising crystal for watt-level lasers at ~1.9 μm, *J. Alloys Compd.*, 2020, **813**, 152176, DOI: **10.1016/j.jallcom.2019.152176**.

20 P. Serna-Gallén, H. Beltrán-Mir and E. Cordoncillo, The unexplored δ-phase of KY₃F₁₀: toward novel Eu³⁺-doped nanoplates with a 'super-diamond' structure for optical applications, *J. Mater. Res. Technol.*, 2021, **15**, 6940–6946, DOI: **10.1016/j.jmrt.2021.11.060**.

21 P. Serna-Gallén, H. Beltrán-Mir, E. Cordoncillo, R. Balda and J. Fernández, A site-selective fluorescence spectroscopy study of the crystal phases of KY₃F₁₀: Leveraging the optical response of Eu³⁺ ions, *J. Alloys Compd.*, 2023, **953**, 170020, DOI: **10.1016/j.jallcom.2023.170020**.

22 P. Serna-Gallén, H. Beltrán-Mir and E. Cordoncillo, The pH-dependent reactions in the sonochemical synthesis of luminescent fluorides: The quest for the formation of KY₃F₁₀ crystal phases, *Ultrason. Sonochem.*, 2022, **87**, 106059, DOI: **10.1016/j.ultsonch.2022.106059**.

23 P. T. Cardew, Ostwald Rule of Stages–Myth or Reality?, *Cryst. Growth Des.*, 2023, **23**, 3958–3969, DOI: **10.1021/acs.cgd.2c00141**.

24 S. Chen, H. Xi and L. Yu, Cross-nucleation between ROY polymorphs, *J. Am. Chem. Soc.*, 2005, **127**, 17439–17444, DOI: **10.1021/ja056072d**.

25 J. Russo and H. Tanaka, Selection mechanism of polymorphs in the crystal nucleation of the Gaussian core model, *Soft Matter*, 2012, **8**, 4206–4215, DOI: **10.1039/c2sm07007c**.

26 S. F. S. P. Looijmans, D. Cavallo, L. Yu and G. W. M. Peters, Cross-Nucleation between Polymorphs: Quantitative Modeling of Kinetics and Morphology, *Cryst. Growth Des.*, 2018, **18**, 3921–3926, DOI: **10.1021/acs.cgd.8b00254**.

27 C. Desgranges and J. Delhommelle, Molecular mechanism for the cross-nucleation between polymorphs, *J. Am. Chem. Soc.*, 2006, **128**, 10368–10369, DOI: **10.1021/ja063218f**.

28 G. Blasse, The europium(III)-fluorine charge-transfer transition, *J. Phys. Chem. Solids*, 1989, **50**, 99, DOI: **10.1016/0022-3697(89)90479-4**.

29 R. R. Reddy, Y. N. Ahammed, K. R. Gopal and D. V. Raghuram, Optical electronegativity and refractive index of materials, *Opt. Mater.*, 1998, **10**, 95–100, DOI: **10.1016/S0925-3467(97)00171-7**.

30 P. Dorenbos, The Eu^{3+} charge transfer energy and the relation with the band gap of compounds, *J. Lumin.*, 2005, **111**, 89–104, DOI: **10.1016/j.jlumin.2004.07.003**.

31 R. T. Wegh, H. Donker, K. D. Oskam and A. Meijerink, Visible quantum cutting in Eu^{3+}-doped gadolinium fluorides via downconversion, *J. Lumin.*, 1999, **82**, 93–104, DOI: **10.1126/science.283.5402.663**.

32 K. Binnemans, Interpretation of europium(III) spectra, *Coord. Chem. Rev.*, 2015, **295**, 1–45, DOI: **10.1016/j.ccr.2015.02.015**.

33 A. Gulzar, J. Xu, P. Yang, F. He and L. Xu, Upconversion processes: Versatile biological applications and biosafety, *Nanoscale*, 2017, **9**, 12248–12282, DOI: **10.1039/c7nr01836c**.

34 P. Serna-Gallén, H. Beltrán-Mir and E. Cordoncillo, Tuning the optical and photoluminescence properties of high efficient Eu^{3+}-doped KY_3F_{10} phosphors by different synthetic approaches, *Opt. Laser Technol.*, 2021, **136**, 106734, DOI: **10.1016/j.optlastec.2020.106734**.

35 T. Yamase, T. Kobayashi, M. Sugeta and H. Naruke, Europium(III) Luminescence and Intramolecular Energy Transfer Studies of Polyoxometalloeuropates, *J. Phys. Chem. A*, 1997, **101**, 5046–5053.

36 R. G. Geitenbeek, H. W. De Wijn and A. Meijerink, Non-Boltzmann Luminescence in $NaYF_4$:Eu^{3+}: Implications for Luminescence Thermometry, *Phys. Rev. Appl.*, 2018, **10**, 1, DOI: **10.1103/PhysRevApplied.10.064006**.

37 S. K. Gupta, C. Reghukumar and R. M. Kadam, Eu^{3+} local site analysis and emission characteristics of novel $Nd_2Zr_2O_7$: Eu phosphor: Insight into the effect of europium concentration on its photoluminescence properties, *RSC Adv.*, 2016, **6**, 53614–53624, DOI: **10.1039/c6ra11698a**.

38 J. Cheng, J. Cheng, S. Zhang, C. Ma, X. Bian and Z. Zhai, Photoluminescence, site occupation and optical thermometry of $Ba_2La_6Y_2(SiO_4)_6O_2$: Eu^{3+} phosphors with high thermal stability, *J. Lumin.*, 2022, **252**, 119265, DOI: **10.1016/j.jlumin.2022.119265**.

39 T. Lan, T. Han, D. Jiang, Y. Wen, X. Y. Sun, Z. Hua, S. Qian, H. Ban, H. Cai, J. Han, H. Liu, S. Liu, L. Ma, L. Qin, J. Ren, G. Tang, Z. Wang, Z. Le Wang and Y. Zhu, Study on the luminescent properties of Eu^{3+}-doped TeO_2-GeO_2-BaO scintillation glasses, *Opt. Mater.*, 2022, **133**, 113000, DOI: **10.1016/j.optmat.2022.113000**.

40 P. Serna-Gallén, H. Beltrán-Mir and E. Cordoncillo, Practical guidance for easily interpreting the emission and physicochemical parameters of Eu^{3+} in solid-state hosts, *Ceram. Int.*, 2023, DOI: **10.1016/j.ceramint.2023.01.141**.

41 D. K. Patel, B. Vishwanadh, V. Sudarsan and S. K. Kulshreshtha, Difference in the Nature of Eu^{3+} Environment in Eu^{3+}-Doped $BaTiO_3$ and $BaSnO_3$, *J. Am. Ceram. Soc.*, 2013, **96**, 3857–3861, DOI: **10.1111/jace.12596**.

42 C. de Mello Donegá, S. A. Junior and G. F. de Sá, Synthesis, luminescence and quantum yields of Eu(III) mixed complexes with 4,4,4-trifluoro-1-phenyl-1,3-butanedione and 1,10-phenanthroline-N-oxide, *J. Alloys Compd.*, 1997, **250**, 422–426, DOI: **10.1016/S0925-8388(96)02562-5**.

43 S. K. Gupta, M. A. Penilla Garcia, J. P. Zuniga and Y. Mao, pH induced size tuning of $Gd_2Hf_2O_7$:Eu^{3+} nanoparticles and its effect on their UV and X-ray excited luminescence, *J. Lumin.*, 2020, **228**, 117605, DOI: **10.1016/j.jlumin.2020.117605**.

44 Y. Tian, B. Chen, R. Hua, J. Sun, L. Cheng, H. Zhong, X. Li, J. Zhang, Y. Zheng, T. Yu, L. Huang and H. Yu, Optical transition, electron-phonon coupling and fluorescent quenching of $La_2(MoO_4)_3$:Eu^{3+} phosphor, *J. Appl. Phys.*, 2011, **109**, 053511, DOI: **10.1063/1.3551584**.

45 M. Luo, X. Sha, B. Chen, X. Zhang, H. Yu, X. Li, J. Zhang, S. Xu, Y. Cao, Y. Wang, X. Wang, Y. Zhang, D. Gao and L. Wang, Optical transition properties, internal quantum efficiencies, and temperature sensing of Er^{3+} doped $BaGd_2O_4$ phosphor with low maximum phonon energy, *J. Am. Ceram. Soc.*, 2022, **105**, 3353–3363, DOI: **10.1111/jace.18299**.

46 J. D. L. Dutra, T. D. Bispo and R. O. Freire, LUMPAC lanthanide luminescence software: Efficient and user friendly, *J. Comput. Chem.*, 2014, **35**, 772–775, DOI: **10.1002/jcc.23542**.

47 A. Ćirić, S. Stojadinović, M. Sekulić and M. D. Dramićanin, JOES: An application software for Judd-Ofelt analysis from Eu^{3+} emission spectra, *J. Lumin.*, 2019, **205**, 351–356, DOI: **10.1016/j.jlumin.2018.09.048**.

48 N. Pathak, S. Mukherjee, B. P. Mandal, A. K. Yadav, S. N. Jha and D. Bhattacharyya, Interplay between local distortion at lattice sites with optical and electrical properties of Eu^{3+}-doped $MNbO_3$ (M = Na and K) compounds, *Mater. Adv.*, 2020, **1**, 2380–2394, DOI: **10.1039/d0ma00335b**.

49 M. M. Fernandes, M. Schmidt, T. Stumpf, C. Walther, D. Bosbach, R. Klenze and T. Fanghänel, Site-selective time-resolved laser fluorescence spectroscopy of Eu^{3+} in calcite, *J. Colloid Interface Sci.*, 2008, **321**, 323–331, DOI: **10.1016/j.jcis.2008.01.017**.

50 Y. Hui, Y. Zhao, S. Zhao, L. Gu, X. Fan, L. Zhu, B. Zou, Y. Wang and X. Cao, Fluorescence of Eu^{3+} as a probe of phase transformation of zirconia, *J. Alloys Compd.*, 2013, **573**, 177–181, DOI: **10.1016/j.jallcom.2013.03.248**.

51 P. Li, Y. Zhang, L. Zhang, F. Li, Y. Guo, Y. Li and W. Gao, Phase Control of Eu^{3+}-Doped YPO_4 Nano−/Microcrystals, *Cryst. Growth Des.*, 2017, **17**, 5935–5944, DOI: **10.1021/acs.cgd.7b01038**.

52 X. Liu, L. Yan and J. Lin, Tunable Photoluminescence and Cathodoluminescence Properties of Eu^{3+}-Doped $LaInO_3$ Nanocrystalline Phosphors, *J. Electrochem. Soc.*, 2009, **156**, 1–6, DOI: **10.1149/1.3002378**.